Deep and Dynamic Metabolic and Structural Imaging in Living Tissues

by

Kunzan Liu

B.S., Tsinghua University (2022)

Submitted to the Department of Electrical Engineering and Computer Science
in partial fulfillment of the requirements for the degree of

MASTER OF SCIENCE

at the

MASSACHUSETTS INSTITUTE OF TECHNOLOGY

May 2024

© 2024 Kunzan Liu. All rights reserved.

The author hereby grants to MIT a nonexclusive, worldwide, irrevocable, royalty-free license to exercise any and all rights under copyright, including to reproduce, preserve, distribute and publicly display copies of the thesis, or release the thesis under an open-access license.

Authored by:	Kunzan Liu Department of Electrical Engineering and Computer Science May 8, 2024
Certified by:	Sixian You Assistant Professor of Electrical Engineering and Computer Science Thesis Supervisor
Accepted by:	Leslie A. Kolodziejski Professor of Electrical Engineering and Computer Science Chair, Department Committee on Graduate Students

Deep and Dynamic Metabolic and Structural Imaging in Living Tissues

by

Kunzan Liu

Submitted to the Department of Electrical Engineering and Computer Science
on May 8, 2024 in partial fulfillment of the requirements for the degree of

MASTER OF SCIENCE

ABSTRACT

Label-free imaging through two-photon autofluorescence (2PAF) of NAD(P)H allows for non-destructive and high-resolution visualization of cellular activities in living systems. However, its application to thick tissues and organoids has been restricted by its limited penetration depth within 300 µm, largely due to tissue scattering at the typical excitation wavelength (∼750 nm) required for NAD(P)H. Here, we demonstrate that the imaging depth for NAD(P)H can be extended to over 700 µm in living engineered human multicellular microtissues by adopting multimode fiber (MMF)-based low-repetition-rate high-peak-power three-photon (3P) excitation of NAD(P)H at 1100 nm. This is achieved by having over 0.5 MW peak power at the band of 1100±25 nm through adaptively modulating multimodal nonlinear pulse propagation with a compact fiber shaper. Moreover, the 8-fold increase in pulse energy at 1100 nm enables faster imaging of monocyte behaviors in the living multicellular models. These results represent a significant advance for deep and dynamic metabolic and structural imaging of intact living biosystems. The modular design (MMF with a slip-on fiber shaper) is anticipated to allow wide adoption of this methodology for demanding *in vivo* and *in vitro* imaging applications, including cancer research, autoimmune diseases, and tissue engineering.

Thesis supervisor: Sixian You
Title: Assistant Professor of Electrical Engineering and Computer Science

Acknowledgments

I would like to express my deepest gratitude to my advisor, Prof. Sixian You. Her extraordinary guidance, support, and mentorship have been instrumental in shaping my research and academic journey.

I extend my heartfelt thanks to my brilliant labmates: Honghao Cao, Dr. Tong Qiu, Dr. Kristina Monakhova, Li-Yu Yu, Kasey Shashaty, Ryan Mei, Cassandra T. Ye, and Jiashu Han. Their collaboration, constructive feedback, and camaraderie have significantly enriched my research experience. I am deeply grateful to Dr. Matthew Yeung, Dr. Steven F. Nagle, and Dr. Haidong Feng for sharing their expertise in electronics and optics. I would also like to sincerely thank Prof. Linda Griffith, Dr. Keith Isaacson, Prof. Eliezer Calo, Prof. Fan Wang, Dr. Michal Tal, and Prof. Roger Kamm for their invaluable insights and guidance on biomedical findings. Additionally, I'm thankful for the collaborative spirit of Dr. Manuel Levy, Dr. Eva Lendaro, Ellen Kan, and Qingying Feng, which has propelled our label-free imaging research forward.

Finally, I am immensely thankful for the unwavering encouragement and understanding provided by my family and friends throughout this journey. Their support has been a constant source of strength.

Contents

Title page 1

Abstract 3

Acknowledgments 5

List of Figures 9

1 Introduction 13

2 SI MMF for high-quality high-peak-power metabolic and structural imaging 15

3 Deep 3PAF NAD(P)H imaging using excitation at 1100 nm 21

4 Deep metabolic and structural imaging of living blood-brain barrier microfluidic model 25

5 Dynamic metabolic and structural imaging of monocyte behaviors *in vitro* 31

6 Conclusion 35

References 37

List of Figures

2.1 **a**, Schematic for working principles. High-energy ultrashort pulses from pump laser (up to 350 nJ, 219 fs) at 1030 nm were injected into the SI MMF, where the propagation of multimodal nonlinear pulses were adaptively modulated by a compact fiber shaper that applies controlled macro-bending. The spectrally-filtered fiber output at 1100 nm is directed to the microscopy system for label-free metabolic and structural imaging, where the imaging signal is used as the feedback for controlling the fiber shaper. **b**, Photograph (middle panel) of the MMF source based on a compact slip-on fiber shaper and its comparison with a US quarter, highlighting the compactness and the modular nature of the MMF source. Left and right panels: illustrative diagrams of the input pulses and the imaging system. Scale bar: 30 mm. **c**, Photograph of the SLAM imaging system. The imaging system was an inverted scanning microscope with 4 detection channels. The data acquisition was achieved by a custom-written LABVIEW software. 18

2.2 Comparison between images acquired with a commercial OPA and with the MMF source at the same site of the mouse whisker pad tissue. The OPA images were captured sequentially at 750 nm and 1300 nm, whereas the MMF source images were captured simultaneously at 1100 nm. Scale bars: 100 µm. OPA: optical parametric amplifier. 19

2.3 Shaping the SI MMF to optimize imaging SNR and resolution. **a**, Comparison of images at the same site of the mouse whisker pad tissue acquired before (initial) and after (optimized) optimizing the fiber shaper, with the same contrast adjustments. Scale bars: 100 µm. Spectral, temporal, and spatial characterizations of the fiber output at the spectral band of 1100±25 nm before (**b**) and after (**c**) optimizing the fiber shaper. The spectra before filtering are also presented (solid blue lines in the left panel). Duration is estimated based on the autocorrelation signals and with the assumption of Gaussian pulse shape. Spatial profiles represent the near-field intensity distributions of the fiber output; numbers denote the correlation with the fundamental LP_{01} mode. 20

3.1 Deep NAD(P)H imaging with 1100 nm MMF source. **a**, Comparison of 2PAF and 3PAF NAD(P)H imaging of intact 3D microvascular network at different depths, applying identical contrast adjustments for the 2PAF and 3PAF images at the same depth. Magnitude of the Fourier transform of individual images are plotted in the insets, indicating differences in the resolution of the images. **b**, 3PAF NAD(P)H imaging of the 3D microvascular network through the entire 720 µm of depth, with 2D images shown at different imaging depths. Scale bars: 100 µm. 22

3.2 **a**, Normalized intensity profiles along the co-registered lines in Fig. 3.1a. **b**, Width of the magnitude of the Fourier transform across different depth in 2PAF and 3PAF NAD(P)H imaging. **c**, Signal intensity of 2PAF and 3PAF as a function of imaging depth measured in the same site of **b**. The effective attenuation lengths (EALs) $\ell_e^{(2)}$ and $\ell_e^{(3)}$ were fitted for 2PAF and 3PAF, respectively. Scale bars: 100 µm. 23

3.3 High peak power improves imaging depth. **a**, Deep SLAM imaging of mouse whisker pad for over 300 µm. **b**, Compare to superficial layers, increasing peak power at deep layers can improve the SNR of imaging. 24

4.1 **a**, Human blood-brain barrier microfluidic models developed with self-assembled vascular endothelial cells, pericytes, and astrocytes. **b**, Immunofluorescence (IF) imaging of stained vascular endothelial cells, pericytes, and astrocytes. Scale bars: 100 µm. 26

4.2 dSLAM for deep metabolic and structural imaging. 3D visualization of THG, NAD(P)H, and FAD signals (**a**) and the merged signals (**b**) for structural and metabolic imaging of the entire 500-µm-deep living blood-brain barrier microfluidic model, comprising vascular endothelial cells, pericytes, and astrocytes. Dashed volume in **b**: a FAD-strong pericyte (yellow arrow) wraps an NAD(P)H-strong vascular endothelial cell (blue arrow). **c**, NAD(P)H and FAD imaging and the resulting map of redox ratio in sub-cellular resolution at the shallowest layer (see Methods for redox calculation). **d, e**, 2D and 3D visualization at different deeper layers, showing the lumen structure and astrocytes extending projections around vascular endothelial cells in the living blood-brain barrier microfluidic model. Scale bars: 100 µm. 28

4.3 **a**, Redox ratio and THG intensity of cells in the volume. Cells cluster into the same type based on their structural and metabolic features. Density (**b**) and redox ratio (**c**), of different cell types at different depths of the living blood-brain barrier microfluidic model. Scale bars: 100 µm. 29

5.1 dSLAM for dynamic metabolic and structural imaging. **a**, Microfludic device setup of *in vitro* imaging of monocyte behaviors in the vasculature network formed by the vascular endothelial cells and fibroblasts. **b**, Trajectories of cells analyzed in the entire 150-s time window. **c**, The statistics of redox ratio of successfully recruited cells, unsuccessfully recruited cells, and moving cells. Scale bars: 50 µm. 32

5.2 **a**, Three motility behaviors of monocytes in the time-lapse imaging, represented by Cell 29, Cell 32, and Cell 40. **b–d**, Speed of the three representative cells during a 25-s time window, with variations in their redox ratio showing the relation between metabolic and motility behaviors. Scale bars: 50 µm. . 33

Chapter 1

Introduction

Capturing the metabolic dynamics of intact and living biosystems is essential in biomedicine from fundamental research to clinical pathology. Label-free two-photon autofluorescence (2PAF) imaging of NAD(P)H and FAD enables non-destructive, high-resolution, and three-dimensional (3D) visualization and characterization of cellular metabolic activities. The use of two-photon (2P) excitation of NAD(P)H imaging has been adopted in major tissue types and diseases for non-invasive assessment of oxidative phosphorylation and glucose catabolism in living cells [1]–[8].

However, NAD(P)H imaging rarely extends beyond 300 µm due to light scattering and out-of-focus background [2], [4], [9]. Compared to the widely adopted 2P-based labeled imaging [10], this problem of limited depth penetration in NAD(P)H imaging is exacerbated by two intrinsic properties of NAD(P)H autofluorophore: (1) 2P cross-section of NAD(P)H is approximately 4 orders of magnitude lower than the commonly used labels such as green fluorescent proteins (GFPs) (10^{-2} GM [11] compared to 10^{2} GM of Calcium Crimson with Ca^{2+} [12]); (2) the excited electronic states of NAD(P)H require more blue-shifted excitation wavelengths compared to existing markers (∼750 nm for NAD(P)H [11], [13] compared to ∼930 nm for GFP [12]), leading to increased scattering in deep tissue.

In this work, we demonstrate the depth limit of NAD(P)H imaging can be significantly alleviated by adopting three-photon (3P) excitation of NAD(P)H at 1100 nm from a multimode fiber (MMF) source. In label-based imaging, it has been proposed and demonstrated that 3P excitation of fluorescent markers can significantly reduce scattering and enhance signal-to-background ratio (SBR) in deeper tissue [14]–[19]. Nevertheless, this has not been successfully extended to label-free NAD(P)H imaging. One pragmatic technical challenge is the lack of existing commercial femtosecond sources near the band of 1100 nm with high peak power and decent beam quality. This work demonstrates the feasibility of using easily accessible MMFs for high-quality deep and dynamic metabolic and structural imaging of living biosystems.

Prior work, abbreviated as SLAM (simultaneous label-free autofluorescence-multiharmonic) imaging, demonstrated the possibility of using photonic crystal fiber (PCF)-based 1110-nm sources for 3P excitation of NAD(P)H [9]. The introduction of 1110-nm excitation enabled simultaneous acquisition of third harmonic generation (THG) originating at the structural interfaces [20]–[22], together with the 3P excitation of NAD(P)H and 2P excitation of FAD, plus second harmonic generation (SHG) from collagen fibers [23], [24]. The combination of these orthogonal contrasts allowed simultaneous visualization of diverse cellular and extracellular components in the unperturbed tissue microenvironment [25]–[29]. Nevertheless, it was not clear how deep SLAM can image into living tissues (the depth was limited to 200 µm due to the energy constraint of excitation pulses) and how widely deployable SLAM could be for the general bioimaging field given the non-trivial PCF and pulse shaper setup.

In this work, we demonstrate for the first time that the depth limit of NAD(P)H imaging can be extended to over 700 µm, using living engineered human multicellular microtissues as test samples, and by adopting MMF-based low-repetition-rate high-peak-power 3P excitation of NAD(P)H at 1100 nm, enabling deep and dynamic SLAM (dSLAM) imaging. The high peak power exceeding 0.5 MW at the band of 1100±25 nm was obtained by adaptively modulating multimodal nonlinear pulse propagation with a compact fiber shaper [30]. Furthermore, the 8-fold increase of pulse energy at 1100 nm allows us to capture faster monocyte behaviors in the engineered human multicellular microtissues *in vitro*. These results and findings represent an important advance towards deeper and faster metabolic and structural imaging of intact living biosystems. We anticipate the flexibility provided by the modular design (step-index (SI) MMF with a slip-on fiber shaper) will allow the proposed imaging methodology to be widely adopted for demanding *in vivo* and *in vitro* imaging applications [31], including cancer research [32]–[35], autoimmune diseases [36], [37], and tissue engineering [38], [39].

Chapter 2

SI MMF for high-quality high-peak-power metabolic and structural imaging

To create a high-peak-power and accessible fiber source at the band of 1100 nm, we chose (1) a standard silica-core SI MMF as the medium for its relatively large mode area and power scalability [40]–[47], and (2) a slip-on compact fiber shaper as the control device for its low cost and ease of use [30] (Fig. 2.1a, b). An SI MMF (Thorlabs, FG025LJA; 25/125 µm, 0.10 NA) of 8.5 cm length was launched by a high-power femtosecond mode-locked ytterbium laser (Light Conversion, Carbide) at 1030 nm with a pulse energy of 350 nJ and a pulse width of 219 fs. Weak focusing was achieved using an achromatic doublet with 100 mm focal length (Thorlabs, AC254-100-B) for fiber coupling with a coupling efficiency of 76%. The output supercontinuum generation pulses were collimated by a 25.4-mm focal length off-axis parabolic mirror (Edmund Optics, 36-586) and spectrally filtered by a 1100±25 nm bandpass filter (Edmund Optics, 85-906). The input peak power up to 1.60 MW (350 nJ pulse energy) is well below the critical power of silica at around 4.7 MW [48].

As expected, the higher nonlinearity associated with 3P processes made THG and NAD(P)H imaging highly susceptible to the deteriorating beam quality and temporal duration that are known to be associated with the MMF output field [49]. Building on the idea of modulating multimodal nonlinear pulse propagation in the recent work [30], we developed a compact version of the fiber shaper for an off-the-shelf 8.5-cm few-mode fiber (25 µm core size) to address the need of better beam quality and shorter temporal duration, to enable deeper and dynamic SLAM imaging (Fig. 2.1b). The fiber shaper was built on our previous device [30] but with a modification to make it smaller. The fiber shaper device was driven by a linear actuator with a 2-phase 4-wire stepper motor, having a motion range of 34 mm and a step size of 0.025 mm. A customized fiber holder was fabricated using acrylic by a laser cutter (Universal, PLS6.75) and was assembled on the actuator slider. A microcontroller unit (Arduino, Uno Rev3) was used to control the stepper motor, with codes programmed in Python and sent from a personal computer (PC). To adapt to the short fiber length for minimizing pulse dispersion, a single high-precision actuator was used, with a minimal bending radius of 5 mm. Compared to the previous 3D printed 5-actuator (to 8-actuator) fiber shaper, the relatively shorter pulses are obtained by using a shorter fiber (30 cm vs 8.5 cm) and the compact laser-cutting-based fiber shaper. The near-Gaussian beam was obtained by modulating the multimodal pulse propagation within a few-mode fiber (25 µm core size) and spectral filtering of the red-shifted wavelengths at 1100 nm. Similar to the previously demonstrated fiber shaper, changing the position of the actuator applies controlled macro-bending on the fiber, which produces local refractive index perturbations and alters the propagation of the nonlinear multimodal pulses, and thus customizes the MMF output in the spectral-temporal-spatial properties. By integrating the signal level of THG imaging as the real-time feedback, the actuator position can be actively adjusted to produce a spectral-temporal-spatial profile that is optimal for 3P imaging (Fig. 2.2).

To investigate the quality of the images that can be obtained with our MMF source, we compare the images out of the optimized MMF source with a state-of-the-art optical parametric amplifier (OPA) (Light Conversion, Cronus-3P) (NAD(P)H/THG using 750 nm/1300 nm from OPA and 1100 nm from MMF) at the same site of the mouse whisker pad tissue. A commercial OPA (Light Conversion, Cronus-3P) emitting pulses at 750 nm (approximately 40 fs) and 1300 nm (46 fs) was also directed to the same microscope system for acquiring reference images. The SLAM microscopy was implemented as an inverted scanning microscope (Fig. 2.1c). A galvanometer mirror pair (ScannerMAX, Saturn-5 Galvo and Saturn-9 Galvo) was used to raster scan the 1100 nm beam out of the MMF. A water immersion objective (Olympus, XLPLN25XWMP2) focused the beam on the imaging plane. A microscope stage (ASI, MS2000) was used to adjust the center of the FOV for mosaic scanning and the focal plane for deep imaging series. The excitation and emission paths were separated by a dichroic mirror (Thorlabs, DMLP650L). The emission signals were further separated into four detection channels using dichroic mirrors (Chroma, T412lpxt, T505lpxr, T570lpxr) and bandpass filters (Chroma, ZET365/20x; Edmund Optics, 84-095; Edmund Optics, 65-159; Semrock, FF01-609/57-25), corresponding to THG, NAD(P)H, SHG, and FAD. Photons were collected by four individual photomultiplier tubes (Hamamatsu, H16201) and signals were translated to images through a custom-written software. The results presented in Fig. 2.1c show that the signal-to-noise ratio (SNR) and the resolution are comparable between the two image sets. The NAD(P)H image out of the MMF source looks even more highly resolved than that of the OPA, but this is very likely to be the consequence of 3P excitation rather than a result of the difference in beam quality.

Since this is an end-to-end adaptive optimization, characterization of the MMF output field in the spectral, temporal, and spatial domains was performed during imaging to provide more information into the mechanism of the improvement. The output pulse spectrum characterization was performed using a NIR spectrometer (Ocean Insight, NIRQuest+1.7). The pulse width was measured using an autocorrelator (Light Conversion, GECO). The near-field output spatial profile was measured using a CMOS-based camera (Mako, G-040B). A representative illustration of this optimization process is presented in Fig. 2.3, where it shows that the signal enhancement of the multiphoton processes can be reliably achieved by adaptively adjusting the position of the single-actuator fiber shaper guided by the signal level of THG imaging. Specifically in this example of imaging the mouse whisker pad tissue, from the initial to the optimized fiber shape, a 1.27-fold increase in band energy and a 1.43-fold reduction in pulse duration, with an improvement of beam spatial profile were obtained (Fig. 2.3b, c; see Methods for correlation calculation). The theoretical signal enhancement for 3P (4.16-fold) and 2P (2.29-fold), calculated using the enhancement in band energy and reduction in pulse duration [50], are comparable to the measured SNR enhancements from Fig. 2.3a, 5.22-fold in 3P processes and 2.70-fold in 2P processes (see Methods for SNR calculation). The slight discrepancy is likely due to the simple assumptions of Gaussian pulse shape and Gaussian beam shape. These results show that, by using the compact fiber shaper on the few-mode SI fiber, a 120-fs near-Gaussian fiber output can be reliably obtained for high-quality high-peak-power metabolic (3P-NADH) and structural (THG) imaging. In addition, the entire wavelength conversion unit is highly compact, modularized, and low-cost (Fig. 2.1b). These results demonstrate the feasibility of using a standard SI MMF with a compact fiber shaper for accessible, high-quality, and high-peak-power excitation at 1100 nm.

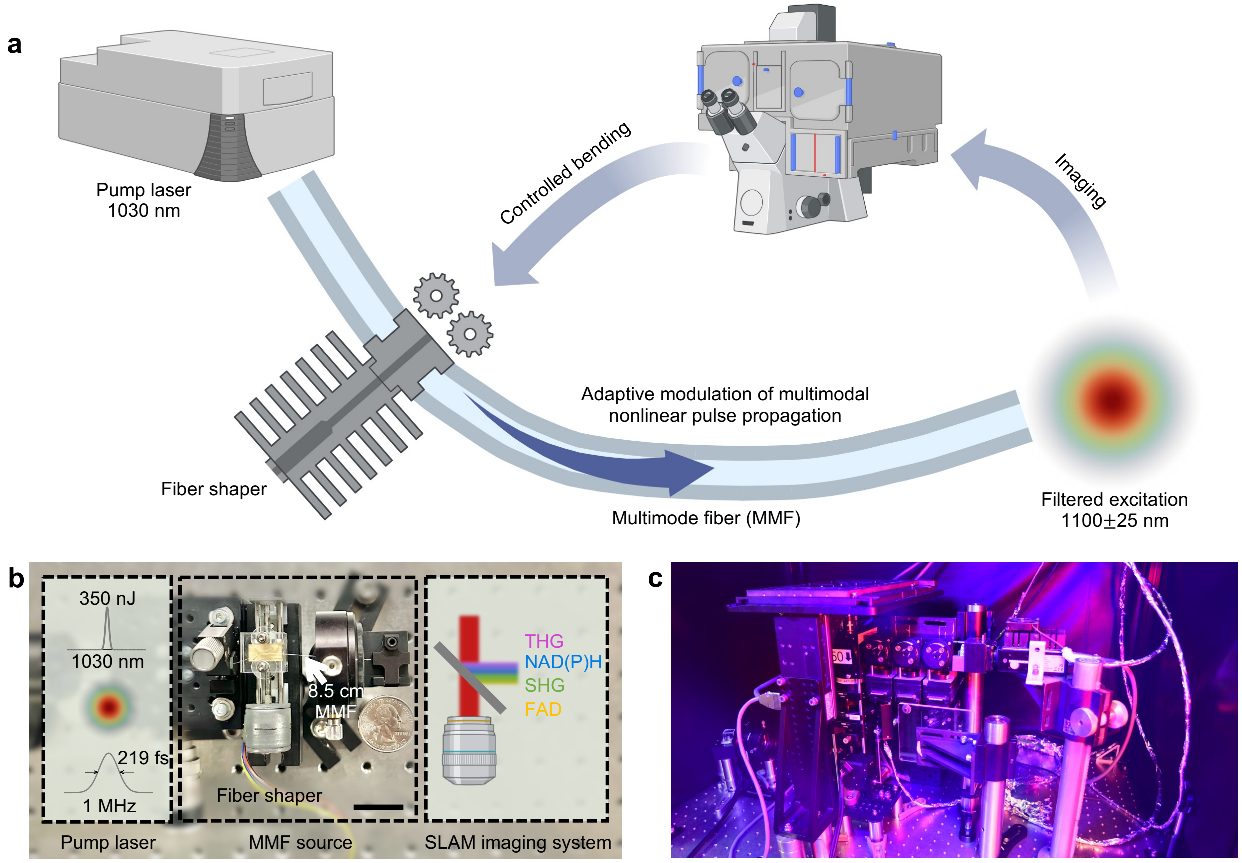
a
Pump laser
1030 nm
Controlled bending
Imaging
Adaptive modulation of multimodal
nonlinear pulse propagation
Fiber shaper
Multimode fiber (MMF)
Filtered excitation
1100±25 nm
b
350 nJ
1030 nm
219 fs
1 MHz
8.5 cm
MMF
Fiber shaper
THG
NAD(P)H
SHG
FAD
Pump laser
MMF source
SLAM imaging system
c

Figure 2.1: **a**, Schematic for working principles. High-energy ultrashort pulses from pump laser (up to 350 nJ, 219 fs) at 1030 nm were injected into the SI MMF, where the propagation of multimodal nonlinear pulses were adaptively modulated by a compact fiber shaper that applies controlled macro-bending. The spectrally-filtered fiber output at 1100 nm is directed to the microscopy system for label-free metabolic and structural imaging, where the imaging signal is used as the feedback for controlling the fiber shaper. **b**, Photograph (middle panel) of the MMF source based on a compact slip-on fiber shaper and its comparison with a US quarter, highlighting the compactness and the modular nature of the MMF source. Left and right panels: illustrative diagrams of the input pulses and the imaging system. Scale bar: 30 mm. **c**, Photograph of the SLAM imaging system. The imaging system was an inverted scanning microscope with 4 detection channels. The data acquisition was achieved by a custom-written LABVIEW software.

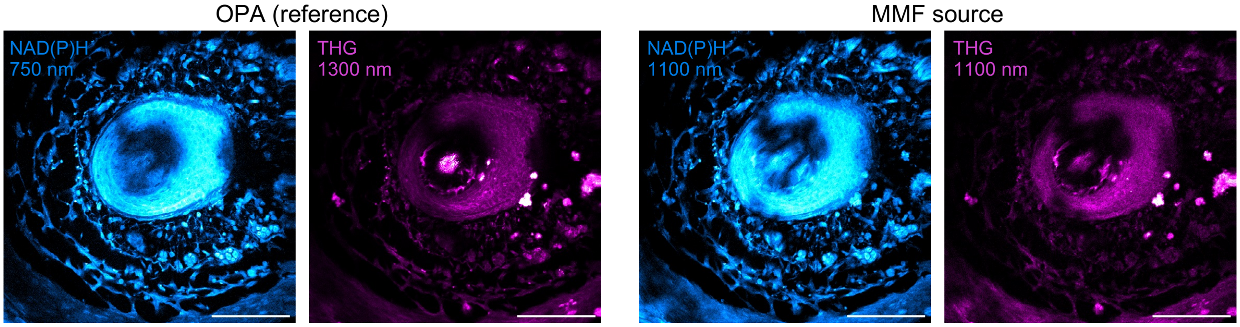
OPA (reference)
MMF source
NAD(P)H
750 nm
THG
1300 nm
NAD(P)H
1100 nm
THG
1100 nm

Figure 2.2: Comparison between images acquired with a commercial OPA and with the MMF source at the same site of the mouse whisker pad tissue. The OPA images were captured sequentially at 750 nm and 1300 nm, whereas the MMF source images were captured simultaneously at 1100 nm. Scale bars: 100 µm. OPA: optical parametric amplifier.

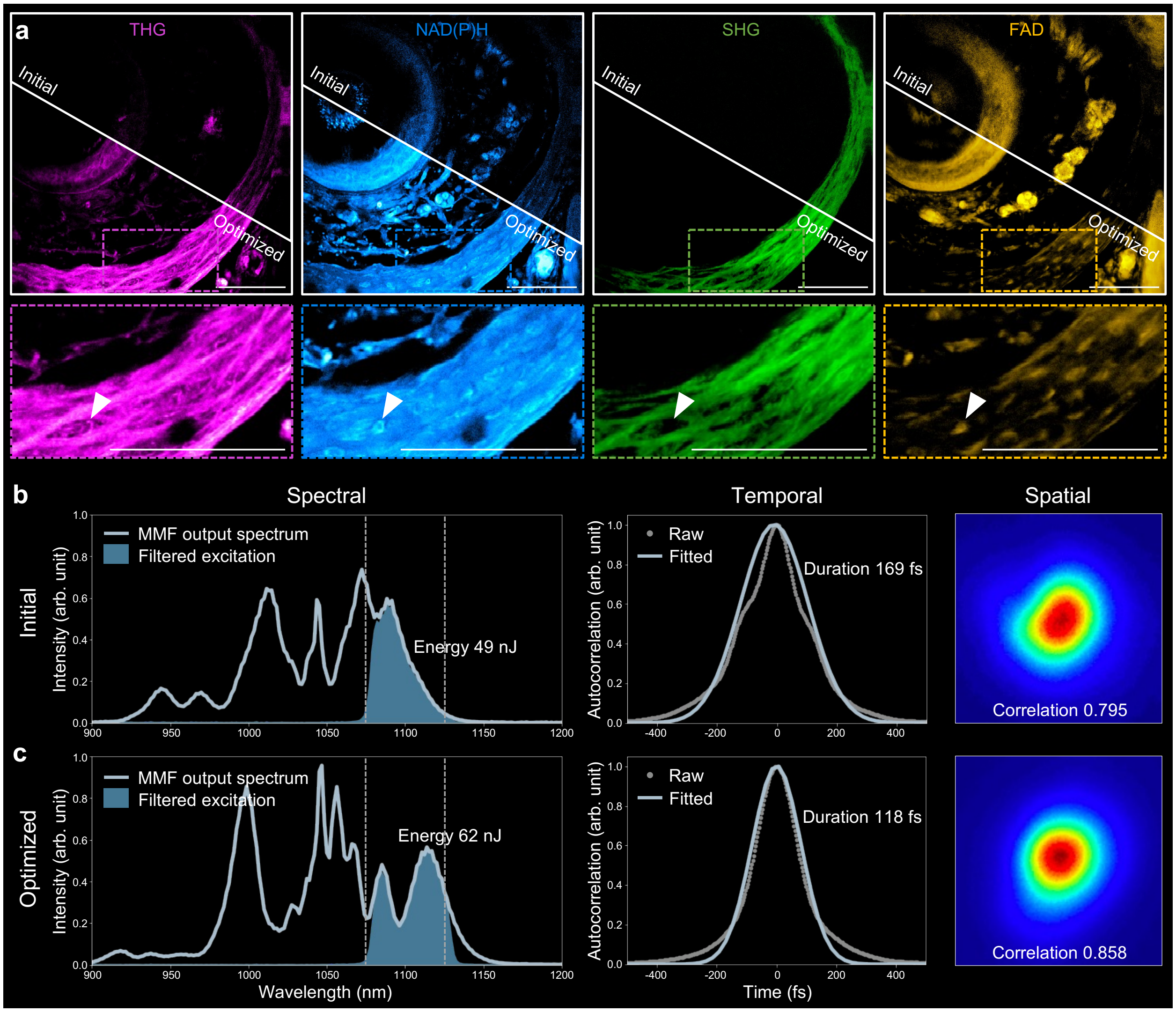

Figure 2.3: Shaping the SI MMF to optimize imaging SNR and resolution. **a**, Comparison of images at the same site of the mouse whisker pad tissue acquired before (initial) and after (optimized) optimizing the fiber shaper, with the same contrast adjustments. Scale bars: 100 µm. Spectral, temporal, and spatial characterizations of the fiber output at the spectral band of 1100 ± 25 nm before (**b**) and after (**c**) optimizing the fiber shaper. The spectra before filtering are also presented (solid blue lines in the left panel). Duration is estimated based on the autocorrelation signals and with the assumption of Gaussian pulse shape. Spatial profiles represent the near-field intensity distributions of the fiber output; numbers denote the correlation with the fundamental LP_{01} mode.

Chapter 3

Deep 3PAF NAD(P)H imaging using excitation at 1100 nm

To investigate the depth limitation of NAD(P)H imaging and the effectiveness of using 1100 nm to extend the depth limit, we performed NAD(P)H autofluorescence imaging with 2P excitation at 750 nm and 3P excitation at 1100 nm. For comparison, the 2PAF NAD(P)H imaging was performed using the signal path from the OPA at 750 nm, and the 3PAF NAD(P)H imaging at the same site was performed using the MMF-based 1100 nm source using a 3D microvascular network [51], [52], with varying pulse energy according to the imaging depths that maintains ∼3 nJ pulse energy at the excitation focus. The microvascular network is an engineered human multicellular microtissue that consists of dense and complex 3D network formed by vascular endothelial cells, which was chosen as test samples since the vascular endothelial cells exhibited stable NAD(P)H signals through the entire 720 µm of depth (Fig. 3.1b).

In superficial layers ($Z \leq 200\,\mu\text{m}$), the NAD(P)H images generated using 2PAF have comparable SNR and resolution as the 3PAF using 1100 nm. However, as the imaging delves deeper, due to the out-of-focus background signal, the SBR degrades much faster in 2PAF (Fig. 3.1a). For example, at the depth of $Z = 600\,\mu\text{m}$, the SBR of 2PAF dropped to 1.12, compared to 6.68 for 3PAF. The low SBR can lead to failure in identifying cells (white arrow in Fig. 3.1a at $Z = 400\,\mu\text{m}$) and structures (lines in Fig. 3.1a at $Z = 600\,\mu\text{m}$, with intensity profiles in Fig. 3.2a).

Next, we quantified the image degradation and signal attenuation of both 2P and 3P nonlinear processes in relation to imaging depth in Fig. 3.2b and 3.2c. The imaging SBR was calculated as the ratio of the average value of the brightest 0.5% pixels and the average value of the pixels in the generated background mask. We observed that a significant contributor to the degradation of the 2PAF NAD(P)H imaging is the overwhelming background and the

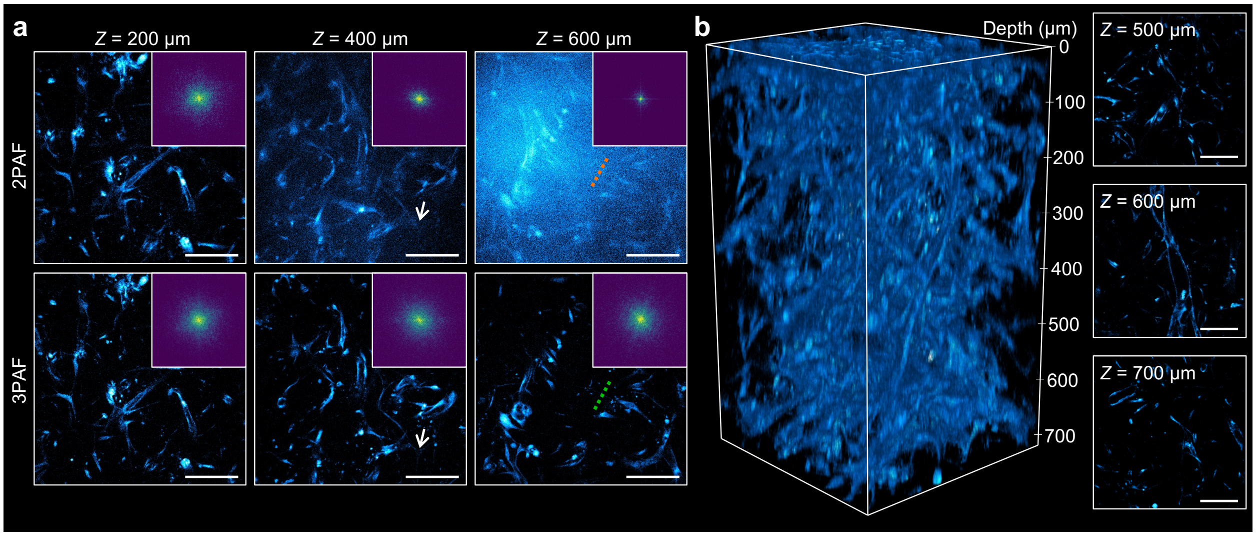

Figure 3.1: Deep NAD(P)H imaging with 1100 nm MMF source. **a**, Comparison of 2PAF and 3PAF NAD(P)H imaging of intact 3D microvascular network at different depths, applying identical contrast adjustments for the 2PAF and 3PAF images at the same depth. Magnitude of the Fourier transform of individual images are plotted in the insets, indicating differences in the resolution of the images. **b**, 3PAF NAD(P)H imaging of the 3D microvascular network through the entire 720 µm of depth, with 2D images shown at different imaging depths. Scale bars: 100 µm.

blurred high-frequency details in the spatial domain of the 2D image slice, which corresponds to a significantly increased dominance of the low-frequency zone and decreased coverage of the high-frequency zone in the frequency domain, as visualized by the spectrum of the Fourier transform shown in the insets of Fig. 3.1a. Qualitatively, we computed and plotted the width of the spectrum of the Fourier transform in Fig. 3.2b across different depths. As the imaging depth increases, the resolution degradation occurs much faster in the 750 nm 2P excitation scheme. In addition, we characterized the effective attenuation lengths (EALs) of NAD(P)H, defined by the depth at which the fluorescence signal attenuates by $1/e^2$ and $1/e^3$ for 2P and 3P imaging, respectively [16]. The EAL of 1100 nm 3PAF NAD(P)H imaging was measured as $\ell_e^{(3)} = 160$ µm, 1.63 times longer than that of $\ell_e^{(2)} = 98$ µm in 750 nm 2PAF (Fig. 3.2c), which benefits from the use of longer excitation wavelength in 3P imaging [14], [15], [17], [53]. These investigations suggest that NAD(P)H imaging in deep tissue requires 1100 nm high-peak-power 3P excitation for high-resolution and high-contrast imaging throughout the entire depth of the 3D microvascular network, underscoring the potential of dSLAM for deep and dynamic metabolic and structural imaging.

We also show that high peak power is needed for deep imaging (Fig. 3.3). In the example of imaging mouse whisker pad tissue, as the imaging get deeper, the SNR dropped expenentially due to the effective attenuation. Therefore, increasing peak power at deep

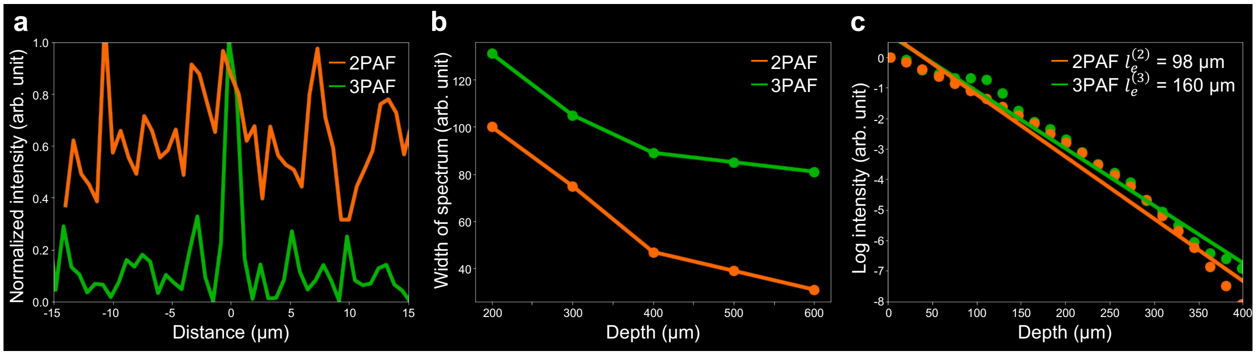

Figure 3.2: **a**, Normalized intensity profiles along the co-registered lines in Fig. 3.1a. **b**, Width of the magnitude of the Fourier transform across different depth in 2PAF and 3PAF NAD(P)H imaging. **c**, Signal intensity of 2PAF and 3PAF as a function of imaging depth measured in the same site of **b**. The effective attenuation lengths (EALs) $\ell_e^{(2)}$ and $\ell_e^{(3)}$ were fitted for 2PAF and 3PAF, respectively. Scale bars: 100 µm.

layers can improve the SNR of imaging and high peak power source is essential for achieving deep imaging.

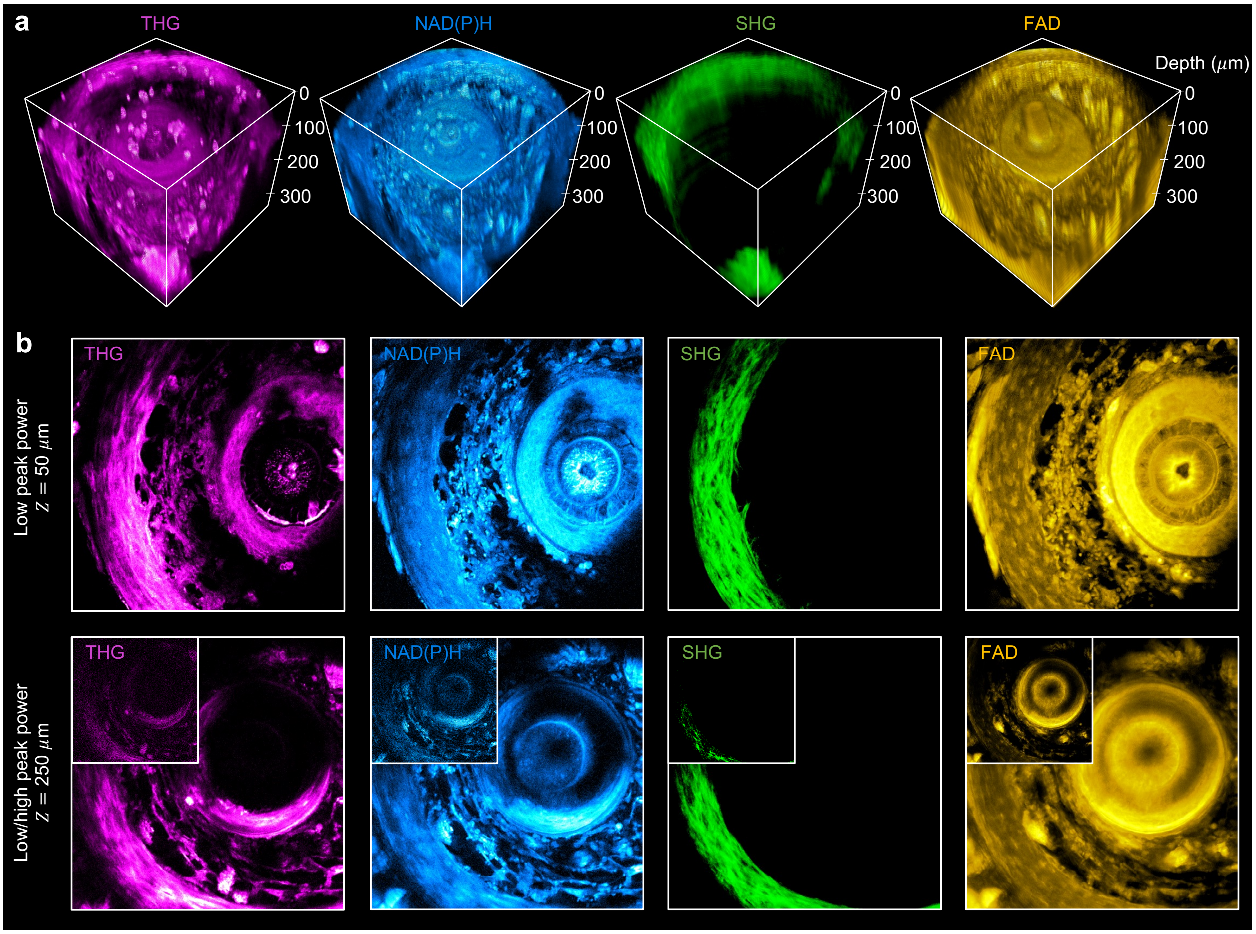
a
THG
NAD(P)H
SHG
FAD
Depth (μm)
0
100
200
300
b
THG
NAD(P)H
SHG
FAD
Low peak power
Z = 50 μm
Low/high peak power
Z = 250 μm

Figure 3.3: High peak power improves imaging depth. **a**, Deep SLAM imaging of mouse whisker pad for over 300 µm. **b**, Compare to superficial layers, increasing peak power at deep layers can improve the SNR of imaging.

Chapter 4

Deep metabolic and structural imaging of living blood-brain barrier microfluidic model

A major motivation for developing the dSLAM imaging platform is to perform non-invasive deep metabolic and structural characterization of living multicellular systems at the subcellular level. To examine the capability of dSLAM for this task, we acquired a 350 µm×350 µm×500 µm image stack of living blood-brain barrier microfluidic models (the entire depth of the model) [54], as shown in Fig. 4.2. Developing and monitoring blood-brain barrier microfluidic models are essential for improving targeted therapies for neurological disorders [54]. Deep label-free metabolic and structural imaging of human blood-brain barrier models *in vitro* could aid the development of therapeutics with improved brain delivery. Here we show that, by using the MMF-based 1100-nm excitation with over 0.5 MW peak power, the deep NAD(P)H imaging integrated with the simultaneously acquired THG and FAD imaging allows 3D redox mapping of the entire intact living human blood-brain barrier model (Fig. 4.2).

The microvascular network of the blood-brain barrier was engineered employing a triculture of primary human astrocytes (ScienCell, 1800), primary human brain pericytes (ScienCell, 1200), and IPSCs-derived vascular endothelial cells (Alstem, iPS11) (Fig. 4.1). Cells were expanded using the following media: Astrocyte Medium (ScienCell, 1801), Pericyte Medium (ScienCell, 1201), VascuLife VEGF Endothelial Medium (Lifeline Cell Technology, LL-0003) supplemented with 10% fetal bovine serum (Thermo Fisher Scientific, 26140-079) and SB 431542 (Selleckchem, S1067). Cells were passaged using TrypLE Express (ThermoFisher, 12604021). The 3D microfluidic co-culture was conducted as described in [55]. For Fig. 4.1b, IF staining for anti-platelet-derived growth factor receptor beta (PDGFR-beta) (Abcam, ab69506; RRID: AB1269704), and anti-glial fibrillary acidic protein (GFAP)

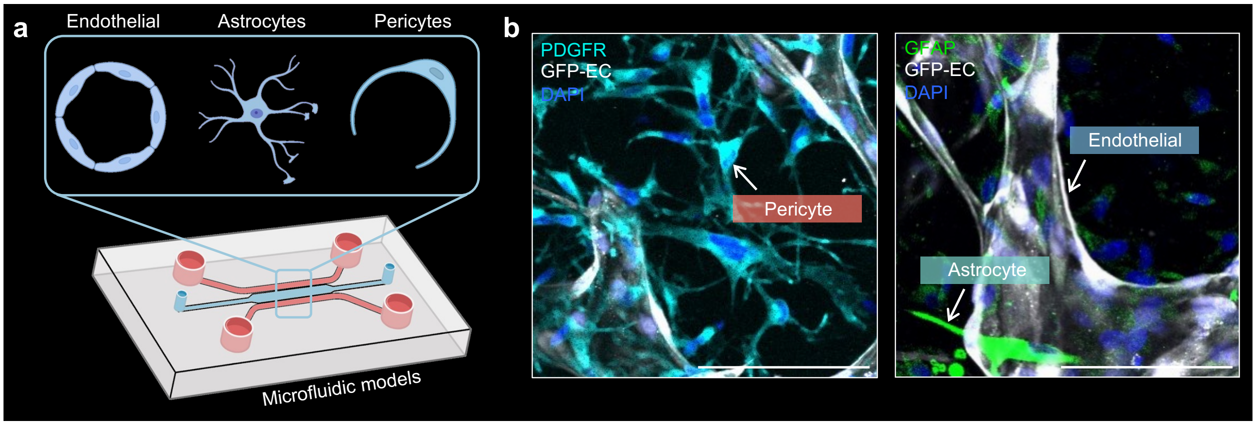

Figure 4.1: **a**, Human blood-brain barrier microfluidic models developed with self-assembled vascular endothelial cells, pericytes, and astrocytes. **b**, Immunofluorescence (IF) imaging of stained vascular endothelial cells, pericytes, and astrocytes. Scale bars: 100 µm.

(Abcam, ab10062; RRID: AB296804) was conducted as described in [54]. 3D visualization from Fiji [56] distinctly shows the three cell types based on their optical signatures in the surrounding fibrin gel (Fig. 4.2a, b, compared with immunofluorescence (IF) imaging of stained cells in Fig. 4.1b). For example, vascular endothelial cells, which are engineered to form a perfusable vasculature (blue arrow in Fig. 4.2b), exhibit high NAD(P)H, consistent with demonstrations that endothelial cells use glycolysis for ATP production [28], [57]–[60]. Pericytes, wrapping around the vasculature (yellow arrow in Fig. 4.2b), are observed to have a high concentration of FAD, likely due to their contractile functions [61]–[63]. Astrocytes, responsible for regulating ion and neurotransmitter concentrations, exhibit strong THG signals, which is in line with previous reports and might be attributed to their complex branched morphology [58], [64]. Further quantification of the redox ratio and the THG signal intensity in Fig. 4.3a shows distinct cell clusters based on their raw optical signatures.

Together with the distinct optical signatures, the deep 3D imaging capability enables non-invasive visualization of the complex multicellular interactions, metabolic states, and depth-dependent variations within the living blood-brain barrier microfluidic model. At the shallowest layer ($Z = 0\,\mu\text{m}$, closest to the cover glass bottom), the cells displayed flat-out morphology that's similar to 2D cell cultures (Fig. 4.2c). As the imaging delves deeper, cells start to exhibit three-dimensional features, such as the forming of the lumen at $Z = 100\,\mu\text{m}$ (Fig. 4.2d, arrow pointing to the lumen of the vasculature network formed by vascular endothelial cells), the wrapping actions of pericytes over vascular endothelial cells at $Z = 120\,\mu\text{m}$ (Fig. 4.2b, dashed volume with zoom-in visualization on the side, with yellow arrow pointing to the pericytes and blue arrow pointing to the vascular endothelial cells), and astrocytes extending projections around vascular endothelial cells at $Z = 468\,\mu\text{m}$

(Fig. 4.2e). Furthermore, deep structural and metabolic imaging reveals depth-dependent metabolic distributions in living cells. For example, as shown in Fig. 4.3c, pericytes in the middle of the blood-brain barrier model (Z=100–400 µm) were observed to have higher FAD intensity compared to the outer layers. This phenomenon may arise from the proximity of the glass chamber at the shallowest and deepest layer of the blood-brain barrier microfluidic model, which could impact the pericyte contractile functions, or limit the growth of pericyte due to the constrained orientation of the vasculature network.

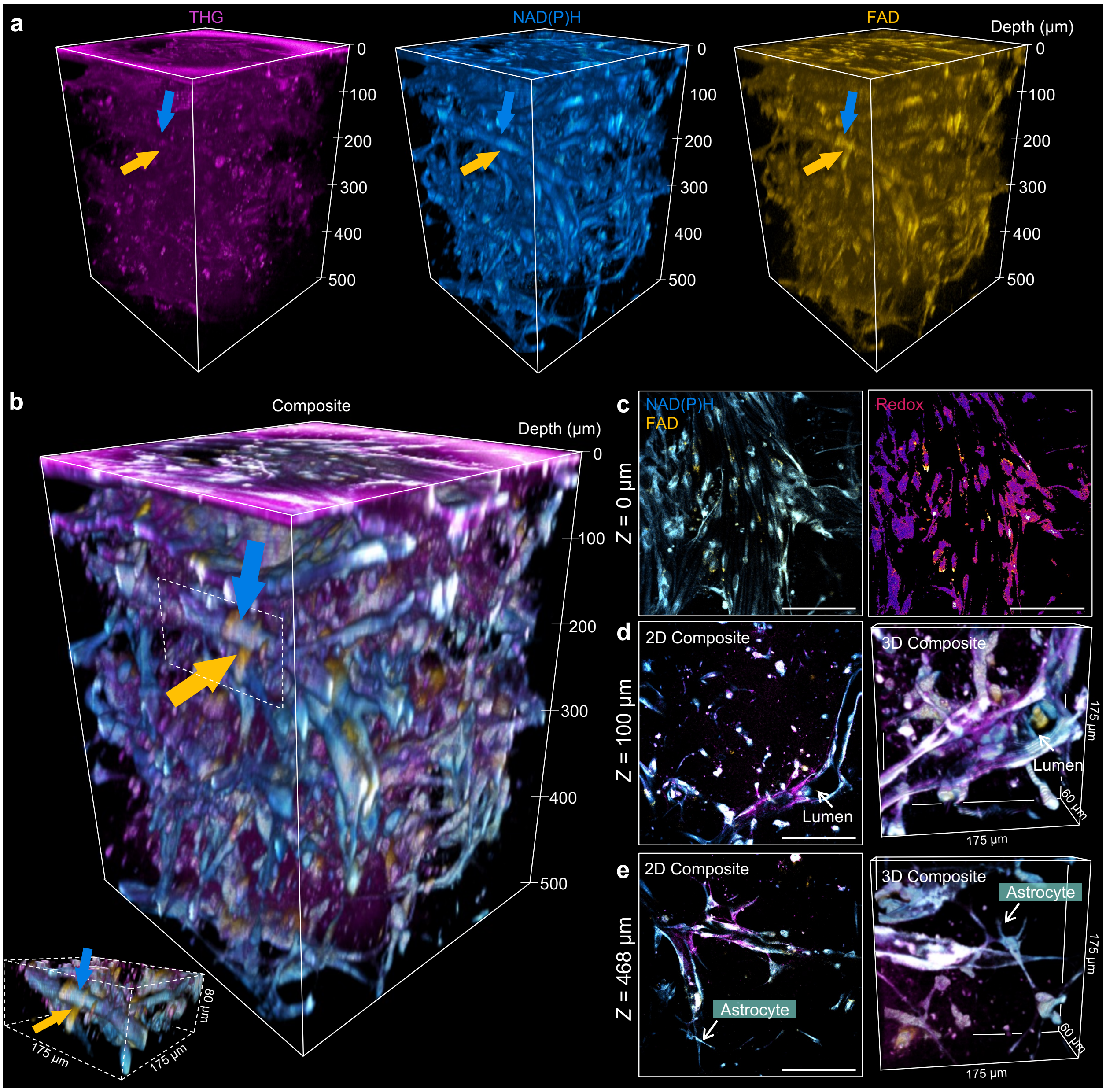
a
THG
NAD(P)H
FAD
Depth (µm)
0
100
200
300
400
500
b
Composite
Depth (µm)
0
100
200
300
400
500
175 µm
175 µm
80 µm
c
NAD(P)H
FAD
Redox
Z = 0 µm
d
2D Composite
3D Composite
Z = 100 µm
Lumen
Lumen
175 µm
175 µm
60 µm
e
2D Composite
3D Composite
Z = 468 µm
Astrocyte
Astrocyte
175 µm
175 µm
60 µm

Figure 4.2: dSLAM for deep metabolic and structural imaging. 3D visualization of THG, NAD(P)H, and FAD signals (**a**) and the merged signals (**b**) for structural and metabolic imaging of the entire 500-µm-deep living blood-brain barrier microfluidic model, comprising vascular endothelial cells, pericytes, and astrocytes. Dashed volume in **b**: a FAD-strong pericyte (yellow arrow) wraps an NAD(P)H-strong vascular endothelial cell (blue arrow). **c**, NAD(P)H and FAD imaging and the resulting map of redox ratio in sub-cellular resolution at the shallowest layer (see Methods for redox calculation). **d, e**, 2D and 3D visualization at different deeper layers, showing the lumen structure and astrocytes extending projections around vascular endothelial cells in the living blood-brain barrier microfluidic model. Scale bars: 100 µm.

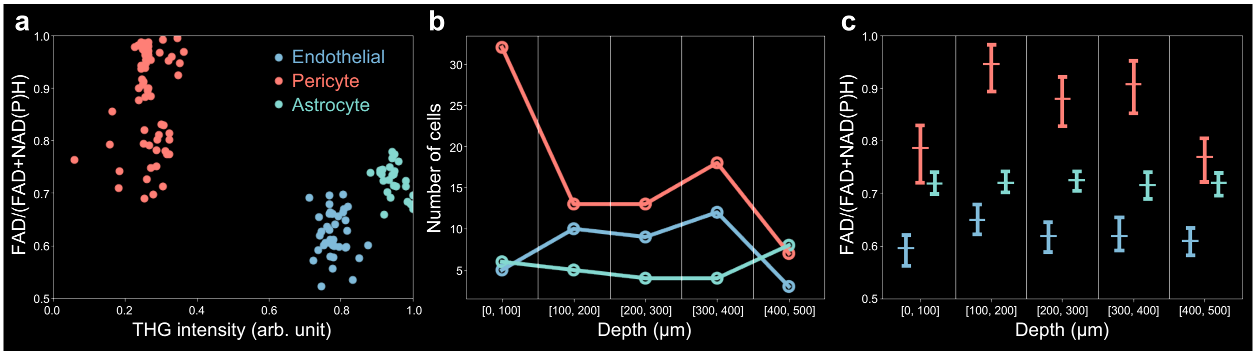

Figure 4.3: **a**, Redox ratio and THG intensity of cells in the volume. Cells cluster into the same type based on their structural and metabolic features. Density (**b**) and redox ratio (**c**), of different cell types at different depths of the living blood-brain barrier microfluidic model. Scale bars: 100 µm.

Chapter 5

Dynamic metabolic and structural imaging of monocyte behaviors *in vitro*

Another motivation for developing a label-free metabolic and structural imaging system is to perform non-invasive imaging of cellular dynamics in living and thick biosystems. Previous SLAM imaging demonstrates the capability of SLAM microscopy on tracking the metabolic dynamics of leukocyte migration *in vivo* up to 40 µm/min [9]. The speed was largely limited by the available peak power (∼40 kW) at the excitation focus. With the peak power of over 0.5 MW out of filtered excitation of the optimized MMF source, we are able to record time-lapse videos at a pixel rate between 0.5–1 MHz, which is ultimately limited by the repetition rate of our pump laser.

To examine the capability of dSLAM for capturing faster dynamics, monocyte behaviors were tracked *in vitro* to mimic the immune cell recruitment process in the living vascular network (Fig. 5.1a) [65], with time-lapse imaging at a pixel rate of 0.5 MHz, which permits a frame rate of 2 Hz and a field-of-view (FOV) of $0.12 \times 0.12\,\mathrm{mm}^2$ for simultaneously monitoring multicellular metabolic and motility behaviors. Human umbilical vein endothelial cells (HUVECs; Angioproteomie, cAP-0001) and normal human lung fibroblasts (NHLFs; Lonza, CC-2512) were cultured in VascuLife VEGF Endothelial Medium and FibroLife S2 Fibroblast Medium (Lifeline Cell Technology, LL-0011), respectively. After the cells were detached with TrypLE Express, they were suspended in a thrombin solution, mixed with fibrinogen, and seeded into a microfluidic device, as previously described [65]. 10 µL of the cell-laden fibrin mix was seeded per device into a central channel that measured approximately 9 mm×3 mm×500 µm, with final cell concentrations of 7 M/mL and 1.5 M/mL for the HUVECs and NHLFs, respectively. Devices were kept in the incubator after gelation, with daily media changes of VascuLife medium for 6 days, until the HUVECs self-assembled into perfusable microvascular networks. Primary human monocytes were isolated from buffy coats

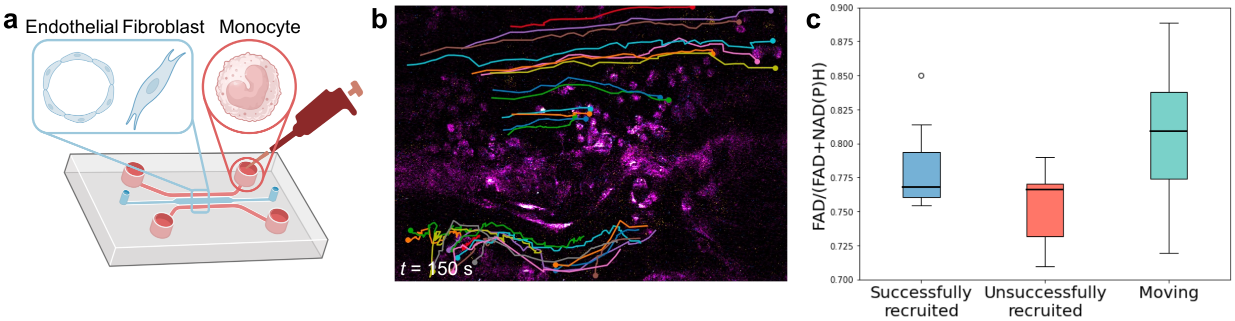

Figure 5.1: dSLAM for dynamic metabolic and structural imaging. **a**, Microfludic device setup of *in vitro* imaging of monocyte behaviors in the vasculature network formed by the vascular endothelial cells and fibroblasts. **b**, Trajectories of cells analyzed in the entire 150-s time window. **c**, The statistics of redox ratio of successfully recruited cells, unsuccessfully recruited cells, and moving cells. Scale bars: 50 µm.

acquired from Massachusetts General Hospital. Monocytes were resuspended at 2 M/mL before addition to microvascular networks.

In Fig. 5.1b, the metabolic activities and motility features of 50 cells were characterized over a 150-s imaging session, with captured speeds exceeding 1000 µm/min (Cell 29 in Fig. 5.2a). We observed a few motility behavioral patterns during this window (Fig. 5.2c). As an example, Cell 29 exhibited rapid movement within the lumen and maintained a redox ratio indicative of a high metabolic state, while Cell 40 remained stationary, with a stable redox ratio of $R_{40} = 0.73$. Interestingly, Cell 32 showed a marked decrease in both speed and redox ratio before adhering to the vasculature. Fig. 5.2a illustrates the speed and metabolic changes of the three representative cells during the monocyte recruitment. To investigate the potential link between cell recruitment and metabolic activity, Fig. 5.1c depicts the redox ratio of stationary and moving cells tracked in Fig. 5.1b, suggesting a lower redox ratio in stationary cells, potentially pointing to increased metabolic activities in monocytes that have attached to the vascular networks. The application of this imaging platform to various living tissue models and pathologies could offer distinctive insights into the metabolic changes accompanying immune cell dynamics within multicellular systems.

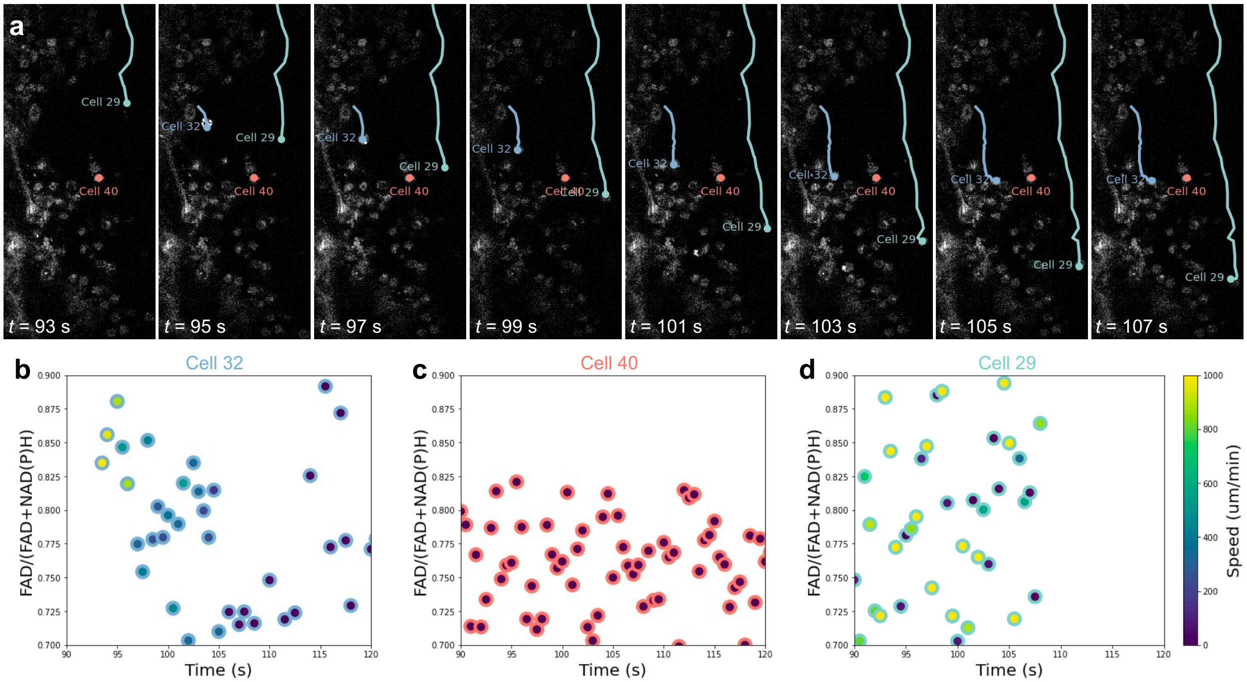

Figure 5.2: **a**, Three motility behaviors of monocytes in the time-lapse imaging, represented by Cell 29, Cell 32, and Cell 40. **b–d**, Speed of the three representative cells during a 25-s time window, with variations in their redox ratio showing the relation between metabolic and motility behaviors. Scale bars: 50 µm.

Chapter 6

Conclusion

The results here demonstrate a significant advancement in the deep and dynamic imaging capabilities of label-free NAD(P)H microscopy in intact living biological systems. By leveraging MMF-based wavelength conversion to generate high-peak-power pulses at 1100±25 nm band, we were able to extend the practical imaging depth of NAD(P)H to 700 µm in living engineered human multicellular microtissues. This enhancement in imaging depth opens up new possibilities for visualizing metabolic processes and structural features in significantly thicker 3D tissue constructs and small model organisms. The ability to observe multicellular interactions and metabolic processes at greater depths with improved imaging speed, holds promise for unraveling the complexities of diseases such as cancer, neurodegenerative disorders, and immune-mediated conditions. Additionally, the utilization of an MMF with a compact slip-on fiber shaper facilitates the delivery of high-peak-power pulses with a near-Gaussian beam profile in a flexible manner, offering potential for miniaturization and widespread adoption compared to prior approaches.

References

[1] I. Georgakoudi, B. C. Jacobson, M. G. Muller, E. E. Sheets, K. Badizadegan, D. L. Carr-Locke, C. P. Crum, C. W. Boone, R. R. Dasari, J. Van Dam, *et al.*, "NAD(P)H and collagen as *in vivo* quantitative fluorescent biomarkers of epithelial precancerous changes," *Cancer Res.*, vol. 62, no. 3, pp. 682–687, 2002.

[2] O. I. Kolenc and K. P. Quinn, "Evaluating cell metabolism through autofluorescence imaging of NAD(P)H and FAD," *Antioxidants & Redox Signaling*, vol. 30, no. 6, pp. 875–889, 2019.

[3] Z. Liu, D. Pouli, C. A. Alonzo, A. Varone, S. Karaliota, K. P. Quinn, K. Münger, K. P. Karalis, and I. Georgakoudi, "Mapping metabolic changes by noninvasive, multiparametric, high-resolution imaging using endogenous contrast," *Sci. Adv.*, vol. 4, no. 3, eaap9302, 2018.

[4] M. C. Skala, K. M. Riching, A. Gendron-Fitzpatrick, J. Eickhoff, K. W. Eliceiri, J. G. White, and N. Ramanujam, "*In vivo* multiphoton microscopy of NADH and FAD redox states, fluorescence lifetimes, and cellular morphology in precancerous epithelia," *Proc. Natl. Acad. Sci. U.S.A.*, vol. 104, no. 49, pp. 19 494–19 499, 2007.

[5] A. J. Walsh, R. S. Cook, H. C. Manning, D. J. Hicks, A. Lafontant, C. L. Arteaga, and M. C. Skala, "Optical metabolic imaging identifies glycolytic levels, subtypes, and early-treatment response in breast cancer," *Cancer Res.*, vol. 73, no. 20, pp. 6164–6174, 2013.

[6] G. R. Gordon, H. B. Choi, R. L. Rungta, G. C. Ellis-Davies, and B. A. MacVicar, "Brain metabolism dictates the polarity of astrocyte control over arterioles," *Nature*, vol. 456, no. 7223, pp. 745–749, 2008.

[7] T. M. Heaster, A. R. Heaton, P. M. Sondel, and M. C. Skala, "Intravital metabolic autofluorescence imaging captures macrophage heterogeneity across normal and cancerous tissue," *Front. Bioeng. Biotechnol.*, vol. 9, p. 644 648, 2021.

[8] A. J. Walsh, K. P. Mueller, K. Tweed, I. Jones, C. M. Walsh, N. J. Piscopo, N. M. Niemi, D. J. Pagliarini, K. Saha, and M. C. Skala, “Classification of T-cell activation via autofluorescence lifetime imaging,” *Nat. Biomed. Eng.*, vol. 5, no. 1, pp. 77–88, 2021.

[9] S. You, H. Tu, E. J. Chaney, Y. Sun, Y. Zhao, A. J. Bower, Y.-Z. Liu, M. Marjanovic, S. Sinha, Y. Pu, *et al.*, “Intravital imaging by simultaneous label-free autofluorescence-multiharmonic microscopy,” *Nat. Commun.*, vol. 9, no. 1, p. 2125, 2018.

[10] F. Helmchen and W. Denk, “Deep tissue two-photon microscopy,” *Nat. Methods*, vol. 2, no. 12, pp. 932–940, 2005.

[11] S. Huang, A. A. Heikal, and W. W. Webb, “Two-photon fluorescence spectroscopy and microscopy of NAD(P)H and flavoprotein,” *Biophys. J.*, vol. 82, no. 5, pp. 2811–2825, 2002.

[12] C. Xu, R. Williams, W. Zipfel, and W. W. Webb, “Multiphoton excitation cross-sections of molecular fluorophores,” *Bioimaging*, vol. 4, no. 3, pp. 198–207, 1996.

[13] W. R. Zipfel, R. M. Williams, R. Christie, A. Y. Nikitin, B. T. Hyman, and W. W. Webb, “Live tissue intrinsic emission microscopy using multiphoton-excited native fluorescence and second harmonic generation,” *Proc. Natl. Acad. Sci. U.S.A.*, vol. 100, no. 12, pp. 7075–7080, 2003.

[14] N. G. Horton, K. Wang, D. Kobat, C. G. Clark, F. W. Wise, C. B. Schaffer, and C. Xu, “*In vivo* three-photon microscopy of subcortical structures within an intact mouse brain,” *Nat. Photon.*, vol. 7, no. 3, pp. 205–209, 2013.

[15] T. Wang and C. Xu, “Three-photon neuronal imaging in deep mouse brain,” *Optica*, vol. 7, no. 8, pp. 947–960, 2020.

[16] K. Choe, Y. Hontani, T. Wang, E. Hebert, D. G. Ouzounov, K. Lai, A. Singh, W. Béguelin, A. M. Melnick, and C. Xu, “Intravital three-photon microscopy allows visualization over the entire depth of mouse lymph nodes,” *Nat. Immunol.*, vol. 23, no. 2, pp. 330–340, 2022.

[17] T. Wang, D. G. Ouzounov, C. Wu, N. G. Horton, B. Zhang, C.-H. Wu, Y. Zhang, M. J. Schnitzer, and C. Xu, “Three-photon imaging of mouse brain structure and function through the intact skull,” *Nat. Methods*, vol. 15, no. 10, pp. 789–792, 2018.

[18] G. Wang, L. Li, X. Liao, S. Wang, J. Mitchell, R. “. Rabel, S. Luo, J. Shi, J. E. Sorrells, R. R. Iyer, *et al.*, “Supercontinuum intrinsic fluorescence imaging heralds ‘free view’ of living systems,” *bioRxiv*, pp. 2024–01, 2024.

[19] G. Wang, L. Li, J. E. Sorrells, J. Chen, and H. Tu, "Gentle label-free nonlinear optical imaging relaxes linear-absorption-mediated triplet," *bioRxiv*, pp. 2023–10, 2023.

[20] B. Weigelin, G.-J. Bakker, and P. Friedl, "Third harmonic generation microscopy of cells and tissue organization," *J. Cell Sci.*, vol. 129, no. 2, pp. 245–255, 2016.

[21] D. Débarre, W. Supatto, A.-M. Pena, A. Fabre, T. Tordjmann, L. Combettes, M.-C. Schanne-Klein, and E. Beaurepaire, "Imaging lipid bodies in cells and tissues using third-harmonic generation microscopy," *Nat. Methods*, vol. 3, no. 1, pp. 47–53, 2006.

[22] M. Yildirim, C. Delepine, D. Feldman, V. A. Pham, S. Chou, J. Ip, A. Nott, L.-H. Tsai, G.-L. Ming, P. T. So, *et al.*, "Label-free three-photon imaging of intact human cerebral organoids for tracking early events in brain development and deficits in Rett syndrome," *Elife*, vol. 11, e78079, 2022.

[23] P. J. Campagnola and L. M. Loew, "Second-harmonic imaging microscopy for visualizing biomolecular arrays in cells, tissues and organisms," *Nat. Biotechnol.*, vol. 21, no. 11, pp. 1356–1360, 2003.

[24] A. Zoumi, A. Yeh, and B. J. Tromberg, "Imaging cells and extracellular matrix *in vivo* by using second-harmonic generation and two-photon excited fluorescence," *Proc. Natl. Acad. Sci. U.S.A.*, vol. 99, no. 17, pp. 11 014–11 019, 2002.

[25] S. You, Y. Sun, E. J. Chaney, Y. Zhao, J. Chen, S. A. Boppart, and H. Tu, "Slide-free virtual histochemistry (Part II): Detection of field cancerization," *Biomed. Opt. Express*, vol. 9, no. 11, pp. 5253–5268, 2018.

[26] S. You, R. Barkalifa, E. J. Chaney, H. Tu, J. Park, J. E. Sorrells, Y. Sun, Y.-Z. Liu, L. Yang, D. Z. Chen, *et al.*, "Label-free visualization and characterization of extracellular vesicles in breast cancer," *Proc. Natl. Acad. Sci. U.S.A.*, vol. 116, no. 48, pp. 24 012–24 018, 2019.

[27] S. You, Y. Sun, L. Yang, J. Park, H. Tu, M. Marjanovic, S. Sinha, and S. A. Boppart, "Real-time intraoperative diagnosis by deep neural network driven multiphoton virtual histology," *npj Precision Oncology*, vol. 3, no. 1, p. 33, 2019.

[28] S. You, E. J. Chaney, H. Tu, Y. Sun, S. Sinha, and S. A. Boppart, "Label-free deep profiling of the tumor microenvironment," *Cancer Res.*, vol. 81, no. 9, pp. 2534–2544, 2021.

[29] J. Park, J. E. Sorrells, E. J. Chaney, A. M. Abdelrahman, J. A. Yonkus, J. L. Leiting, H. Nelson, J. J. Harrington, E. Aksamitiene, M. Marjanovic, *et al.*, "*In vivo* label-free optical signatures of chemotherapy response in human pancreatic ductal adenocarcinoma patient-derived xenografts," *Commun. Biol.*, vol. 6, no. 1, p. 980, 2023.

[30] T. Qiu, H. Cao, K. Liu, L.-Y. Yu, M. Levy, E. Lendaro, F. Wang, and S. You, "Spectral-temporal-spatial customization via modulating multimodal nonlinear pulse propagation," *Nat. Commun.*, vol. 15, no. 1, p. 2031, 2024.

[31] C. Xu and F. Wise, "Recent advances in fibre lasers for nonlinear microscopy," *Nat. Photon.*, vol. 7, no. 11, pp. 875–882, 2013.

[32] D. Entenberg, M. H. Oktay, and J. S. Condeelis, "Intravital imaging to study cancer progression and metastasis," *Nat. Rev. Cancer*, vol. 23, no. 1, pp. 25–42, 2023.

[33] A. J. Walsh, R. S. Cook, M. E. Sanders, L. Aurisicchio, G. Ciliberto, C. L. Arteaga, and M. C. Skala, "Quantitative optical imaging of primary tumor organoid metabolism predicts drug response in breast cancer," *Cancer Res.*, vol. 74, no. 18, pp. 5184–5194, 2014.

[34] P. Friedl and K. Wolf, "Tumour-cell invasion and migration: Diversity and escape mechanisms," *Nat. Rev. Cancer*, vol. 3, no. 5, pp. 362–374, 2003.

[35] J. Condeelis and J. W. Pollard, "Macrophages: Obligate partners for tumor cell migration, invasion, and metastasis," *Cell*, vol. 124, no. 2, pp. 263–266, 2006.

[36] D. L. Pham, A. A. Gillette, J. Riendeau, K. Wiech, E. C. Guzman, R. Datta, and M. C. Skala, "Perspectives on label-free microscopy of heterogeneous and dynamic biological systems," *J. Biomed. Opt.*, vol. 29, no. S2, S22702–S22702, 2025.

[37] P. Friedl, "Prespecification and plasticity: Shifting mechanisms of cell migration," *Curr. Opin. Cell Biol.*, vol. 16, no. 1, pp. 14–23, 2004.

[38] I. K. Zervantonakis, S. K. Hughes-Alford, J. L. Charest, J. S. Condeelis, F. B. Gertler, and R. D. Kamm, "Three-dimensional microfluidic model for tumor cell intravasation and endothelial barrier function," *Proc. Natl. Acad. Sci. U.S.A.*, vol. 109, no. 34, pp. 13 515–13 520, 2012.

[39] L. G. Griffith and M. A. Swartz, "Capturing complex 3D tissue physiology *in vitro*," *Nat. Rev. Mol. Cell Biol.*, vol. 7, no. 3, pp. 211–224, 2006.

[40] L. G. Wright, W. H. Renninger, D. N. Christodoulides, and F. W. Wise, "Nonlinear multimode photonics: Nonlinear optics with many degrees of freedom," *Optica*, vol. 9, no. 7, pp. 824–841, 2022.

[41] K. Krupa, A. Tonello, A. Barthélémy, T. Mansuryan, V. Couderc, G. Millot, P. Grelu, D. Modotto, S. A. Babin, and S. Wabnitz, "Multimode nonlinear fiber optics, a spatiotemporal avenue," *APL Photonics*, vol. 4, no. 11, p. 110 901, 2019.

[42] L. G. Wright, F. O. Wu, D. N. Christodoulides, and F. W. Wise, "Physics of highly multimode nonlinear optical systems," *Nat. Phys.*, vol. 18, no. 9, pp. 1018–1030, 2022.

[43] L. G. Wright, D. N. Christodoulides, and F. W. Wise, "Spatiotemporal mode-locking in multimode fiber lasers," *Science*, vol. 358, no. 6359, pp. 94–97, 2017.

[44] X. Wei, J. C. Jing, Y. Shen, and L. V. Wang, "Harnessing a multi-dimensional fibre laser using genetic wavefront shaping," *Light Sci. Appl.*, vol. 9, no. 1, p. 149, 2020.

[45] Y. Ding, X. Xiao, K. Liu, S. Fan, X. Zhang, and C. Yang, "Spatiotemporal mode-locking in lasers with large modal dispersion," *Phys. Rev. Lett.*, vol. 126, no. 9, p. 093 901, 2021.

[46] K. Ji, I. Davidson, J. Sahu, D. J. Richardson, S. Wabnitz, and M. Guasoni, "Mode attraction, rejection and control in nonlinear multimode optics," *Nat. Commun.*, vol. 14, no. 1, p. 7704, 2023.

[47] K. Krupa, A. Tonello, B. M. Shalaby, M. Fabert, A. Barthélémy, G. Millot, S. Wabnitz, and V. Couderc, "Spatial beam self-cleaning in multimode fibres," *Nat. Photon.*, vol. 11, no. 4, pp. 237–241, 2017.

[48] A. Dubietis, G. Tamošauskas, R. Šuminas, V. Jukna, and A. Couairon, "Ultrafast supercontinuum generation in bulk condensed media," *Lithuanian Journal of Physics*, vol. 57, no. 3, pp. 113–157, 2017.

[49] C. Xu and W. W. Webb, "Multiphoton excitation of molecular fluorophores and nonlinear laser microscopy," in *Topics in Fluorescence Spectroscopy: Volume 5: Nonlinear and Two-Photon-Induced Fluorescence*, Springer, 2002, pp. 471–540.

[50] Y. Hontani, F. Xia, and C. Xu, "Multicolor three-photon fluorescence imaging with single-wavelength excitation deep in mouse brain," *Sci. Adv.*, vol. 7, no. 12, eabf3531, 2021.

[51] S. Zhang, Z. Wan, and R. D. Kamm, "Vascularized organoids on a chip: Strategies for engineering organoids with functional vasculature," *Lab on a Chip*, vol. 21, no. 3, pp. 473–488, 2021.

[52] Z. Wan, A. X. Zhong, S. Zhang, G. Pavlou, M. F. Coughlin, S. E. Shelton, H. T. Nguyen, J. H. Lorch, D. A. Barbie, and R. D. Kamm, "A robust method for perfusable microvascular network formation *in vitro*," *Small Methods*, vol. 6, no. 6, p. 2 200 143, 2022.

[53] D. G. Ouzounov, T. Wang, M. Wang, D. D. Feng, N. G. Horton, J. C. Cruz-Hernández, Y.-T. Cheng, J. Reimer, A. S. Tolias, N. Nishimura, *et al.*, "*In vivo* three-photon imaging of activity of GCaMP6-labeled neurons deep in intact mouse brain," *Nat. Methods*, vol. 14, no. 4, pp. 388–390, 2017.

[54] C. Hajal, G. S. Offeddu, Y. Shin, S. Zhang, O. Morozova, D. Hickman, C. G. Knutson, and R. D. Kamm, “Engineered human blood-brain barrier microfluidic model for vascular permeability analyses,” *Nat. Protoc.*, vol. 17, no. 1, pp. 95–128, 2022.

[55] E. C. Ko, S. Spitz, F. M. Pramotton, O. M. Barr, C. Xu, G. Pavlou, S. Zhang, A. Tsai, A. Maaser-Hecker, M. Jorfi, *et al.*, “Accelerating the *in vitro* emulation of Alzheimer’s disease-associated phenotypes using a novel 3D blood-brain barrier neurosphere coculture model,” *Front. Bioeng. Biotechnol.*, vol. 11, 2023.

[56] J. Schindelin, I. Arganda-Carreras, E. Frise, V. Kaynig, M. Longair, T. Pietzsch, S. Preibisch, C. Rueden, S. Saalfeld, B. Schmid, *et al.*, “Fiji: An open-source platform for biological-image analysis,” *Nat. Methods*, vol. 9, no. 7, pp. 676–682, 2012.

[57] I. Georgakoudi and K. P. Quinn, “Optical imaging using endogenous contrast to assess metabolic state,” *Annu. Rev. Biomed. Eng.*, vol. 14, pp. 351–367, 2012.

[58] M. Pochechuev, A. Lanin, I. Kelmanson, D. Bilan, D. Kotova, A. Chebotarev, V. Tarabykin, A. Fedotov, V. Belousov, and A. Zheltikov, “Stain-free subcellular-resolution astrocyte imaging using third-harmonic generation,” *Opt. Lett.*, vol. 44, no. 12, pp. 3166–3169, 2019.

[59] M. Quintero, S. L. Colombo, A. Godfrey, and S. Moncada, “Mitochondria as signaling organelles in the vascular endothelium,” *Proc. Natl. Acad. Sci. U.S.A.*, vol. 103, no. 14, pp. 5379–5384, 2006.

[60] K. D. Falkenberg, K. Rohlenova, Y. Luo, and P. Carmeliet, “The metabolic engine of endothelial cells,” *Nat. Metab.*, vol. 1, no. 10, pp. 937–946, 2019.

[61] C. M. Peppiatt, C. Howarth, P. Mobbs, and D. Attwell, “Bidirectional control of CNS capillary diameter by pericytes,” *Nature*, vol. 443, no. 7112, pp. 700–704, 2006.

[62] C. N. Hall, C. Reynell, B. Gesslein, N. B. Hamilton, A. Mishra, B. A. Sutherland, F. M. O’Farrell, A. M. Buchan, M. Lauritzen, and D. Attwell, “Capillary pericytes regulate cerebral blood flow in health and disease,” *Nature*, vol. 508, no. 7494, pp. 55–60, 2014.

[63] F. Fernández-Klett, N. Offenhauser, U. Dirnagl, J. Priller, and U. Lindauer, “Pericytes in capillaries are contractile *in vivo*, but arterioles mediate functional hyperemia in the mouse brain,” *Proc. Natl. Acad. Sci. U.S.A.*, vol. 107, no. 51, pp. 22 290–22 295, 2010.

[64] S. Witte, A. Negrean, J. C. Lodder, C. P. De Kock, G. Testa Silva, H. D. Mansvelder, and M. Louise Groot, “Label-free live brain imaging and targeted patching with third-harmonic generation microscopy,” *Proc. Natl. Acad. Sci. U.S.A.*, vol. 108, no. 15, pp. 5970–5975, 2011.

[65] S. Zhang, Z. Wan, G. Pavlou, A. X. Zhong, L. Xu, and R. D. Kamm, “Interstitial flow promotes the formation of functional microvascular networks in vitro through upregulation of matrix metalloproteinase-2,” *Adv. Funct. Mater.*, vol. 32, no. 43, p. 2 206 767, 2022.